Next Generation QTAIM for the Photochemical Ring-Opening Reactions of Oxirane

Xin Bin[1], Alireza Azizi[1], Tianlv Xu[1], Steven R. Kirk[1*], Michael Filatov[1,2] and Samantha Jenkins[1*]

[1]*Key Laboratory of Chemical Biology and Traditional Chinese Medicine Research and Key Laboratory of Resource Fine-Processing and Advanced Materials of Hunan Province of MOE, College of Chemistry and Chemical Engineering, Hunan Normal University, Changsha, Hunan 410081, China*

[2]*Department of Chemistry, Ulsan National Institute of Science and Technology (UNIST), 50 UNIST-gil, Ulsan44919, Korea*

email: steven.kirk@cantab.net
email: mike.filatov@gmail.com
email: samanthajsuman@gmail.com

The conical intersections corresponding to the C-O and C-C ring opening were optimized and the reaction paths traversing these intersections were obtained. Investigation of the C-O ring opening revealed that when traversing the lowest energy conical intersection the reaction path returns to the closed ring geometry. The C-O path traversing the intersection featuring torsion of terminal CH_2 group however, led to a ring-opened geometry, an H-shift and the formation of acetaldehyde that can undergo further dissociation. The observation of different reaction paths was explained by the 3-D paths from QTAIM that defined the most preferred direction of electronic motion that precisely tracked the mechanisms of bond breaking and formation throughout the photo-reactions. The size, orientation and location of these most preferred 3-D paths indicated the extent and direction of motion of atoms, bonds and the degree of torsion or planarity of a bond indicating a predictive ability.

Introduction

The oxirane molecule, despite comprising one of the simplest three-membered rings, can go through monomolecular thermal and photochemical ring-opening reactions that lead to a variety of ring-openings and fragmentations. Robert Gomer and W. Albert Noyes investigated the photochemistry mechanisms of ethylene oxide[1]. Independent of the reaction conditions, the main reaction involves the formation of two radical fragments (CH_3• and CHO) and the sensitization increases the amount of stable acetaldehyde in the primary photolytic processes of oxirane[2]. The main reaction oxirane molecule presents four possible reaction pathways for the oxirane molecule: opening of the cycle via a one-bond rupture (C-O or C-C) including face to face cleavage and conrotatory and disrotatory C-C bond cleavages. The one-bond rupture (C-O or C-C) yields two different intermediates, cycle breaking by a simultaneous two-bond rupture leads either to the formation of ethylene and atomic oxygen and formaldehyde plus a carbenic methylene, see **Scheme 1**. The study by Bigot *et. al*. indicated that the smallest energetic barrier from oxirane ground state (S_0) found in the C-O bond cleavage (2 eV)[3,4].

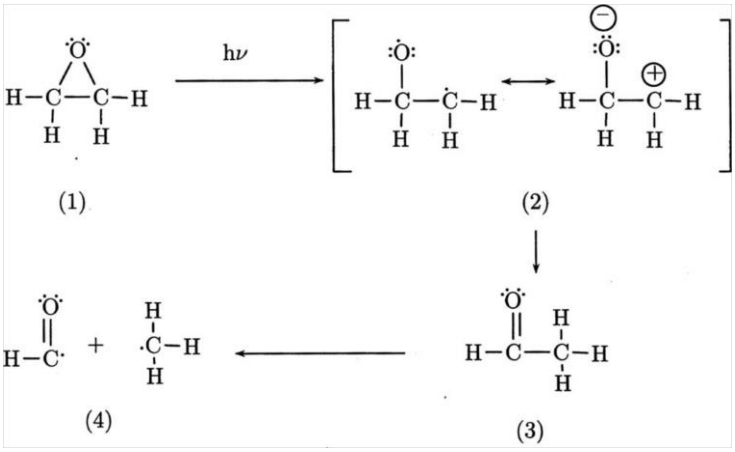

Scheme 1. Conventional mechanism of the photochemical ring-opening in oxirane.

The C-C bond rupture modes requires a high activation energy: 3.6 eV for the face-to-face process, 3.8 eV for the conrotatory mode and 4.1 eV for the disrotatory in thermal reactivity. The easiest and most efficient pathway appears to be C-O bond cleavage, whether in the ^{1}nzWA* or in the ^{3}nzWA* state. In the singlet state, two less likely although competitive processes are C-C bond cleavages in the face-to-face or conrotatory motion in photochemical reactivity[3,4]. It would however, produce a dichotomy since the nature of the substituent can influence both the C-C and C-O bonds cleavage for substituted oxiranes[5–7].

Alkyl substitutions favor C-O bond cleavage both photo-chemically and thermally and aryl substitutions conversely, favor C-C bond breaking which yields 1,3-dipolar species as primary products[5]. The time-dependent density-functional theory (TDDFT) was previously applied for the oxirane photochemical reaction and examined the potential energy curves and surfaces for the symmetric ring-opening of oxirane to assess difficulties[8]. Then a mixed time-dependent density-functional theory Tamm-Dancoff approximation/classical trajectory surface-hopping (TDDFT TDA/SH) approach was used to confirm the main experimentally derived Gomer-Noyes mechanism for the photochemical C-O ring-opening of oxirane

and find excitation into the other excited state leads predominantly to rapid ring-opening (cyclic-C_2H_4O→•CH_2CH_2O•) while one of the lowest two excited states is photo-chemically relatively inert[9]. Tests were undertaken of Wang–Ziegler non-collinear SF(spin-flip)-TDDFT within the Tamm–Dancoff approximation for describing the avoided crossing in the C_{2v} C-C ring-opening reaction of oxirane and for describing the conical intersection relevant for the more asymmetrical C-O ring-opening reaction of oxirane[10]. The transition origins of electronic excitations identified by quantified natural transition orbital (QNTO) analysis can be used to connect potential energy surfaces from to their behavior across a wide range of molecular geometries and applied to oxirane[11].

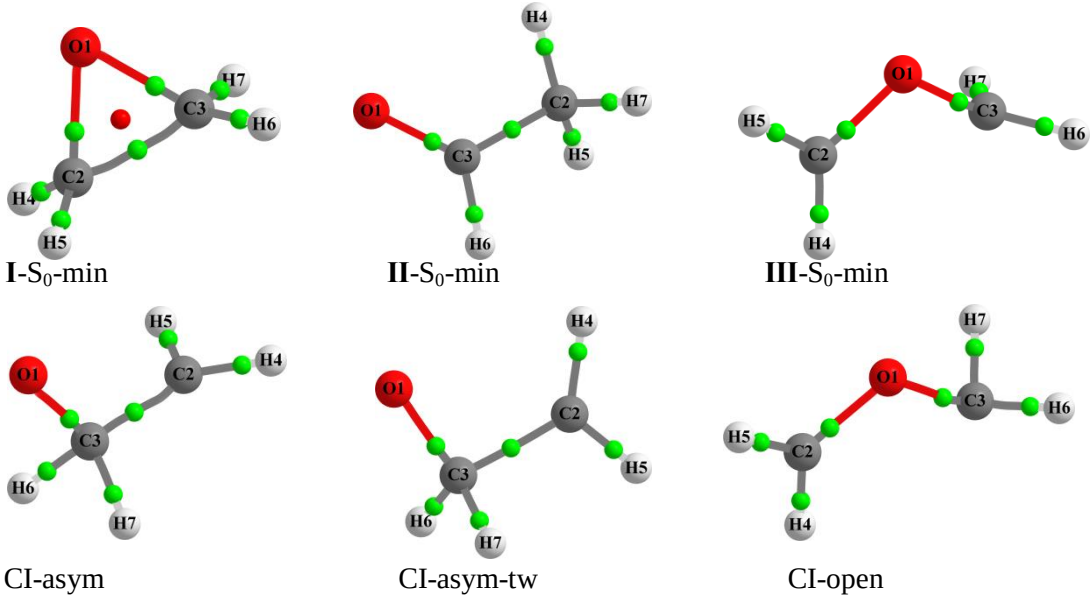

Scheme 2. The molecular graphs and atomic numbering schemes of the oxirane ring-opening reaction along the minimum energy path (MEP) corresponding to FC→ CI-asym → CH_3CHO, FC → CI-asym-tw → CH_3CHO and FC → CI-open → CH_2OCH_2 are shown in top, middle and bottom sub-figures respectively. The FC, CI and CH_3CHO (CH_2OCH_2) molecular graphs indicated in the left, middle and right panels respectively. The undecorated green and red spheres denote the bond critical points (*BCPs*) and ring critical points (*RCPs*) respectively.

Earlier, we used next generation quantum theory of atoms in molecules (QTAIM) to investigate photochemical ring-opening reactions. In particular, the factors underlying two possible pathways for the Dihydrocostunolide (DHCL)[12] as well as the factors underlying the experimentally observed branching ratio (70:30) of the (1,3-cyclohexadiene) CHD→HT (1,3,5-hexatriene)[13]. Useful factors from QTAIM were the ability to prove the existence of an attractive interaction between the ends of the fissile σ-bond of CHD that steered the photochemical ring-opening reaction predominantly in the direction of restoration of the ring. This attractive interaction was quantified in terms of a "stickiness" using the total local energy density $H(\mathbf{r_b})$ in terms of a long weak interaction that obtained the stickiness measured as a degree of covalent character, see theory section 2.1. For the photochemical ring-opening reaction of DHCL oscillations in the chemical character of the fissile bond were found for the reaction pathway that steered the reaction back to reactant before and after the conical intersection. Conversely, this behavior was absent for the other pathway that led forward to the product. For both the CHD and DHCL investigations the bond-path framework set $\mathbb{B}_{0,1}$ = $\{(\boldsymbol{p_0},\boldsymbol{p_1}),(\boldsymbol{q_0},\boldsymbol{q_1}),(\boldsymbol{r_0},\boldsymbol{r_1})\}$, where a bond comprises three strands for a given electronic state, was better able to

quantify the changing bonding character during the reactions that scalar QTAIM analysis using the minimal definition of bonding, i.e. the bond-path (***r***), see theory section 2.2. Other scalar QTAIM approaches include, most notably, IQA (Interacting Quantum Atoms)[14]. In addition, earlier work demonstrated a strong preference to avoid the spontaneous creation or destruction of a strong bond (shared-shell bond critical points (*BCP*s)). Instead it was found that these processes should occur via intermediate weaker (closed-shell bond critical points (*BCP*s))[15].

In this investigation on both the S_0 and S_1 states, we shall also use the 3-D bonding of the next generation QTAIM to explain the mechanisms of oxirane asymmetric ring-opening that involves C2-O1/C3-O1 bond cleavage, see the top and middle sub-figures of **Scheme 2.** In addition, we will examine the symmetric ring-opening (C2-C3 bond cleavage), see the bottom sub-figure of **Scheme 2**.

2. Theory and Methods

2.1 QTAIM and stress tensor BCP properties; ellipticity ε, total local energy density H($\mathbf{r_b}$) and stress tensor eigenvalue $\lambda_{3\sigma} < 0$

We use QTAIM[16] and the stress tensor analysis that utilizes higher derivatives of $\rho(\mathbf{r_b})$ in effect, acting as a 'magnifying lens' on the $\rho(\mathbf{r_b})$ derived properties of the wave-function to identify critical points in the total electronic charge density distribution $\rho(\mathbf{r})$ by analyzing the gradient vector field $\nabla\rho(\mathbf{r})$. These critical points can further be divided into four types of topologically stable critical points according to the set of ordered eigenvalues $\lambda_1 < \lambda_2 < \lambda_3$, with corresponding eigenvectors $\underline{\mathbf{e}}_1$, $\underline{\mathbf{e}}_2$, $\underline{\mathbf{e}}_3$ of the Hessian matrix. The Hessian of the total electronic charge density $\rho(\mathbf{r})$ is defined as the matrix of partial second derivatives with respect to the spatial coordinates. These critical points are labeled using the notation (R, ω) where R is the rank of the Hessian matrix, the number of distinct non-zero eigenvalues and ω is the signature (the algebraic sum of the signs of the eigenvalues); the (3, -3) [nuclear critical point (*NCP*), a local maximum generally corresponding to a nuclear location], (3, -1) and (3, 1) [saddle points, called bond critical points (*BCP*) and ring critical points (*RCP*), respectively] and (3, 3) [the cage critical points (*CCP*)]. In the limit that the forces on the nuclei become vanishingly small, an atomic interaction line[17] becomes a bond-path, although not necessarily a chemical bond[18] with the complete set of critical points and the bond-paths of a molecule being referred to as the molecular graph.

The eigenvector $\underline{\mathbf{e}}_3$ indicates the direction of the bond-path at the *BCP*, the most and least preferred directions of electron accumulation are $\underline{\mathbf{e}}_2$ and $\underline{\mathbf{e}}_1$, respectively[19–21] The ellipticity, ε provides the relative accumulation of $\rho(\mathbf{r_b})$ in the two directions perpendicular to the bond-path at a *BCP*, defined as $\varepsilon = |\lambda_1|/|\lambda_2| - 1$ where λ_1 and λ_2 are negative eigenvalues of the corresponding eigenvectors $\underline{\mathbf{e}}_1$ and $\underline{\mathbf{e}}_2$ respectively. Recently, the 11-cis retinal was investigated and subjected to clockwise and counter-clockwise torsions ±θ, where we

demonstrated that the $\underline{\mathbf{e}}_2$ eigenvector of the torsional *BCP* corresponded to the preferred +θ direction of rotation defined by the PES profile[22]. The total local energy density $H(\mathbf{r}_b)$[23,24]

$$H(\mathbf{r}_b) = G(\mathbf{r}_b) + V(\mathbf{r}_b), \qquad \textbf{(1)}$$

where $G(\mathbf{r}_b)$ and $V(\mathbf{r}_b)$ in equation (**1)** are the local kinetic and potential energy densities at a *BCP*, defines a degree of covalent character: A negative value for $H(\mathbf{r}_b) < 0$ for the closed-shell interaction, a value of the Laplacian $\nabla^2\rho(\mathbf{r}_b) > 0$, indicates a *BCP* with a degree of covalent character and conversely a positive value of $H(\mathbf{r}_b) > 0$ reveals a lack of covalent character for the closed-shell *BCP*. A shared-shell *BCP* always possesses both Laplacian $\nabla^2\rho(\mathbf{r}_b) < 0$ and $H(\mathbf{r}_b) < 0$.

Therefore, we will investigate the presence of intermediate weaker closed-shell *BCP*s during the process of the oxirane ring-opening reactions for each of the three candidate pathways **(a)**, **(b)** or **(c)** shown in **Scheme 2**. The presence or absence of an intermediate weaker bonding interaction indicates the preference or lack of for the particular pathway.

2.2 QTAIM bond-path properties; BPL, the eigenvector-following paths and the bond-path framework set $\mathbb{B}_{0,1} = \{(\boldsymbol{p}_0,\boldsymbol{p}_1),(\boldsymbol{q}_0,\boldsymbol{q}_1),(\boldsymbol{r}_0,\boldsymbol{r}_1)\}$

The bond-path length (BPL) is defined as the length of the path traced out by the $\underline{\mathbf{e}}_3$ eigenvector of the Hessian of the total charge density $\rho(\mathbf{r})$, passing through the *BCP*, along which $\rho(\mathbf{r})$ is locally maximal with respect to any neighboring paths. The bond-path curvature is a dimensionless ratio separating two bonded nuclei and is defined as:

$$(\text{BPL} - \text{GBL})/\text{GBL} \qquad \textbf{(2)}$$

where the geometric bond length (GBL) refers to the inter-nuclear separation. The BPL can exceed the GBL for weak or strained bonds existing in unusual bonding environments[25]. For 3-D bond-paths, there are minor and major radii of bonding curvature specified by the directions of $\underline{\mathbf{e}}_2$ and $\underline{\mathbf{e}}_1$ respectively.[26]

We refer to the next-generation QTAIM interpretation of the chemical bond as the *bond-path framework set*[27], denoted by $\mathbb{B}$, where $\mathbb{B} = \{\boldsymbol{p},\boldsymbol{q},\boldsymbol{r}\}$ with the consequence that for a given electronic state a bond is comprised of three 'linkages'; ***p***, ***q*** and ***r*** associated with the $\underline{\mathbf{e}}_1$, $\underline{\mathbf{e}}_2$ and $\underline{\mathbf{e}}_3$ eigenvectors, respectively. Where the ***p***, ***q*** and ***r*** are 3-D paths constructed from the values of the least ($\underline{\mathbf{e}}_1$) and most ($\underline{\mathbf{e}}_2$) preferred directions of electronic charge density accumulation $\rho(\mathbf{r})$ along the bond-path, referred to as (***r***). It should be noted that the direction of the ***p***-, ***q***- and ***r***-paths always remain orthogonal to each other since they are constructed from the $\underline{\mathbf{e}}_1$, $\underline{\mathbf{e}}_2$ and $\underline{\mathbf{e}}_3$ eigenvectors respectively.

The ellipticity ε is used a scaling factor in the construction of the ***p***- and ***q***-paths:

$$\boldsymbol{p}_i = \boldsymbol{r}_i + \varepsilon_i \underline{\mathbf{e}}_{\mathbf{1},i} \quad \textbf{(3a)}$$

$$\boldsymbol{q}_i = \boldsymbol{r}_i + \varepsilon_i \underline{\mathbf{e}}_{\mathbf{2},i} \quad \textbf{(3b)}$$

The lengths of the ***p***- and ***q***-paths are defined as the *eigenvector-following paths* $\mathbb{H}^*$ or $\mathbb{H}$**:**

$$\mathbb{H}^* = \sum_{i=1}^{n-1} |\boldsymbol{p}_{i+1} - \boldsymbol{p}_i| \quad \textbf{(4a)}$$

$$\mathbb{H} = \sum_{i=1}^{n-1} |\boldsymbol{q}_{i+1} - \boldsymbol{q}_i| \quad \textbf{(4b)}$$

In the limit of vanishing ellipticity $\varepsilon = 0$, *for all* steps *i* along the bond-path then $\mathbb{H}$ = BPL. In addition, the scaling factor, the ellipticity ε_i is identical in equation (**3a)** and equation **(3b)**. The variation of the ellipticity ε along the bond-path with the S_0 and S_1 states is provided in the **Supplementary Materials S1.** The ***p***- and ***q***-paths are always unique even when the lengths of $\mathbb{H}^*$ and $\mathbb{H}$ are the same or very similar since the ***p***- and ***q***-paths traverse different regions of space. The ***p***- and ***q***-paths, the *BCP* ellipticity ε and stress tensor $\lambda_{3\sigma}$ (see section 2.1) are provided in the **Supplementary Materials S2-S4** respectively.

Analogous to the bond-path curvature, see equation **(2)**, a dimensionless *fractional* version ($\mathbb{H}_f$) of the eigenvector-following path $\mathbb{H}$ can be defined as:

$$\mathbb{H}_f = (\mathbb{H} - \text{BPL})/\text{BPL} \quad \textbf{(5)}$$

A similar expressions for $\mathbb{H}^*_f$ can be derived using the $\underline{\mathbf{e}}_1$ eigenvector.

An in-depth discussion of the eigenvector-following paths $\mathbb{H}^*$ and $\mathbb{H}$ including the choice of the ellipticity ε_i as the scaling factor is provided in the **Supplementary Materials S5**. Here we will use the fractional form $\mathbb{H}_f$ that is a dimensionless ratio. Two paths are associated with the $\underline{\mathbf{e}}_2$ (***q*** *and* ***q***') eigenvector because $\underline{\mathbf{e}}_2 = -\underline{\mathbf{e}}_2$ lie in the same plane for the same point on the bond-path (***r***), correspondingly there are two paths associated with the $\underline{\mathbf{e}}_1$ (***p*** and ***p***').

We will focus on the most preferred the ***q***- and ***q***'-paths to track precisely the mechanisms of bond breaking and formation throughout the photo-reactions. We will refer to the orbital-like *packet* shapes that the pair of ***q***- and ***q***'-paths form along the *BCP* as a {***q***,***q'***} path-packet. The size, orientation and location of the {***q***,***q'***} path-packets indicate how much, which direction and whether a bond-path is twisted or linear. **T**he 3-D {***q***,***q'***} path-packets will be used to follow and anticipate *BCP* and bond-path rupture associated with a the C2-O1 *BCP*, C3-O1 *BCP*, C2-C3 *BCP* and the H7 *NCP* transfer processes for the three MEPs, see section 4.3, **Scheme 2**, **Figure 1**. In particular, we will track the torsion of the bond-path (***r***) that may occur for the C2-O1 *BCP* or C3-O1 *BCP*, i.e. comprising two atoms species. This torsion will be indicated by the

presence of perpendicular packets of {***q***,***q'***}-paths either side of the *BCP* along the bond-path (***r***). If a single long {***q***,***q'***}-path packet is found along the bond-path that envelopes the *BCP* then this is likely to indicate an easier (sliding) motion of the *BCP*, bond-path and associated *NCP*s than for the twisted bond-path or a {***q***,***q'***}-path packet localized to the *BCP*. Extremely long {***q***,***q'***}-paths indicate the imminent rupture caused by the coalescence of a *BCP* with the associated *RCP*.

3. Computational Details

Quantum chemical calculations were carried out using the state-interaction state-averaged spin-restricted ensemble-referenced Kohn-Sham (SI-SA-REKS, or SSR) method[28–30]. The SSR method enables one to describe electron correlation effects arising in due to multi-reference character of the ground and excited electronic states through the use of ensemble density functional theory[28,29]. The SSR method has been rigorously tested in the past and proved to be capable of describing the potential energy surfaces (PESs) of the ground and excited electronic states with an accuracy matching the most advanced multi-reference wavefunction methods, including the crossings between the PESs the so-called conical intersections[31–33].
Here, the SSR method is used in connection with the ωPBEh range-separated hybrid density functional[34] and the 6-31G* basis set[35]. The SSR-ωPBEh/6-31G* calculations were carried out using the beta-testing version of the TeraChem quantum chemical program (v1.92P, release 7f19a3bb8334)[36–40]. The geometries of the ground S_0 and first excited state S_1 minima were optimized using the DL-FIND module[41] in connection with the SSR analytic gradient technique[30] The geometries of the S_0/S_1 conical intersections (CIs) were optimized using the CIOpt program[42] interfaced with TeraChem. The minimum energy pathways (MEPs) of the oxirane dissociation reactions were optimized using the nudged elastic band (NEB) method[43] with fixed end points as implemented in the DL-FIND module[41].

4. Results and discussions

4.1. Analysis of the S_1 and S_0 states minimum energy pathways of the oxirane ring-opening reaction

Using the methodology described above the ring opening reaction of oxirane in the S_1 state was investigated. The optimized geometries of the ground state (S_0) and the first excited state (S_1) minima and the S_1/S_0 conical intersections (C.I.s) are presented in **Figure 1**.

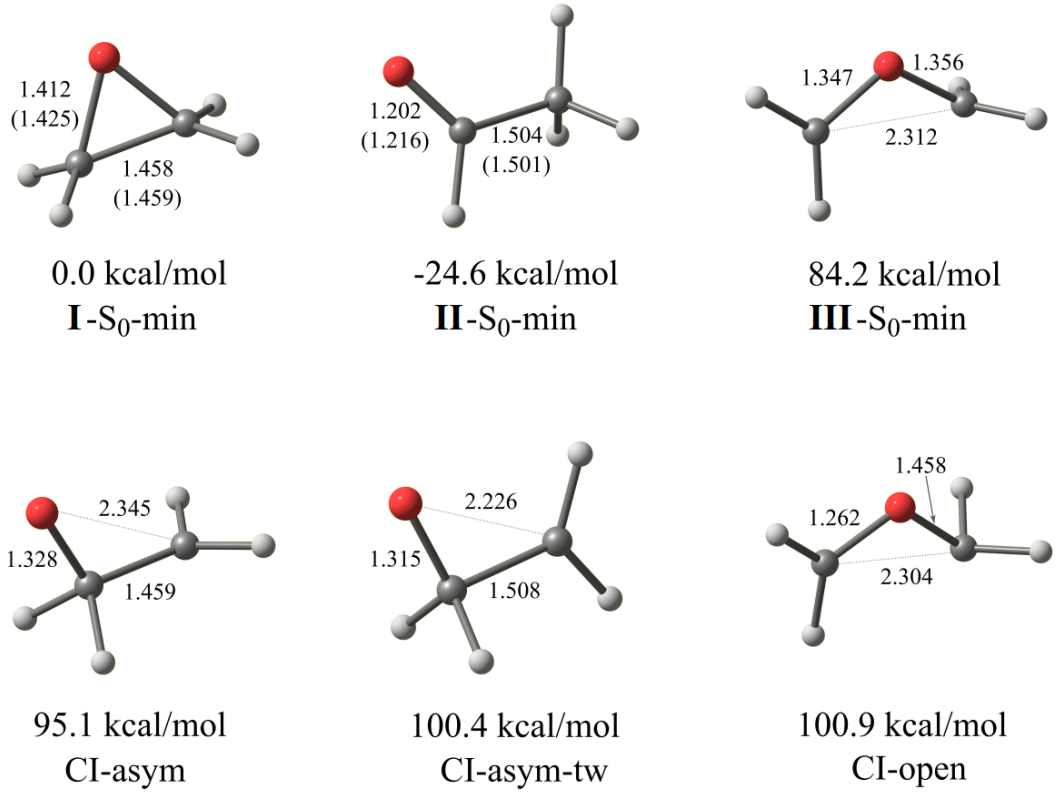

Figure 1. Equilibrium geometries of the S_0 species and the S_1/S_0 conical intersections optimized for ring opening reaction of oxirane in this investigation. Oxirane (**I**), acetaldehyde (**II**), and didehydromethoxymethylene diradical (**III**) geometries are optimized in the S_0 state using the SSR-ωPBEh/6-31G* method are shown in the upper panel and the geometries of the S_1/S_0 conical intersections (C.I.s) in the lower panel. The optimized and experimental bond-lengths (Å) of the key bonds and interatomic separations are shown outside/inside the parentheses, the relative energies ΔE (w.r.t. **I**-S_0 minimum) are presented in kcal/mol.

The equilibrium S_0 geometries of oxirane (**I**), acetaldehyde (**II**), and didehydromethoxymethylene diradical (**III**) optimized with the SSR-ωPBEh/6-31G* method are compared with the available experimental data[44,45] shown parenthetically in **Figure 1**. There is a reasonable agreement between the theoretical and experimental lengths of the C-C and C-O bonds for all the species. The S_0 state of **I** lies 24.6 kcal/mol higher than the S_0 state of **II**. The didehydromethoxymethylene diradical obtained by breaking of the basal C-C bond of **I** is extremely unstable and lies 84.2 kcal/mol above the S_0 state of oxirane.

The excited electronic states of **I** were calculated by the SSR-ωPBEh/6-31G* and the TD-ωPBEh/6-31G* methods at the S_0 equilibrium geometry shown in **Figure 1**. Both computational methods predict that the lowest (S_1) excited state of **I** is obtained by a one-electron transition from the oxygen lone pair orbital (n) to the σ^*-type orbital. The frontier orbitals from the conventional DFT ωPBEh/6-31G* calculation are compared with the natural orbitals obtained from the SSR-ωPBEh/6-31G* relaxed density matrix in **Figure 2**. In the case of TD-DFT, the lowest vertical excitation energy (8.74 eV) is due to the HOMO→LUMO+1 transition. According to TD-DFT the next excited state, S_2, is at 9.36 eV (HOMO→LUMO+2) and the HOMO→LUMO transition is at 9.68 eV (S_3). The SSR method predicts the S_1 state due to the $n \rightarrow \sigma^*$ transition at 8.96 eV, which agrees with the S_1 state from TD-DFT, see **Figure 2**.

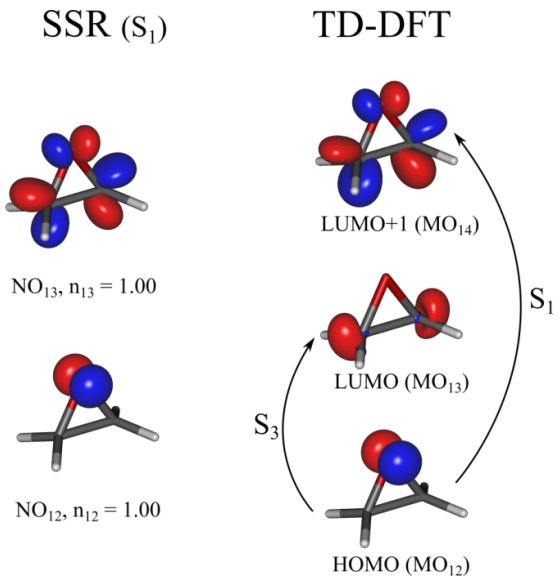

Figure 2. Natural orbitals obtained from the SSR-ωPBEh/6-31G* relaxed density matrix of the S_1 state (left panel) and the frontier orbitals from the KS DFT ωPBEh/6-31G* calculation (right panel). Two lowest orbital transitions from the TD- ωPBEh/6-31G* calculation are shown in the right panel by round arrows.

As population of the σ^*-type orbital results in weakening of both the C-O and C-C bonds, the S_1/S_0 C.I.s were optimized with the SSR-ωPBEh/6-31G* method for both bond breaking pathways. The lowest energy C.I., CI-asym at 95.1 kcal/mol w.r.t. the **I**-S_0-min energy, corresponds to breaking of one of the C-O bonds, see **Figure 1**. At the CI-asym geometry, both CH_2 groups are coplanar, which does not seem favorable for hydrogen transfer from the CH_2O fragment to terminal CH_2. To inspect whether there exists another C.I. geometry that favors the H-transfer, a C.I. corresponding to C2-O1 bond breaking and featuring the terminal CH_2 group twisted through ca. 90°, CI-asym-tw, was optimized. The CI-asym-tw is only 5.3 kcal/mol less stable than the CI-asym and is deemed mechanistically important for the ring opening reaction. Yet another C.I. optimized in this investigation, CI-open, corresponds to breaking of the C2-C3 bond. This C.I. is almost isoenergetic with the CI-asym-tw (100.9 kcal/mol vs. 100.4 kcal/mol) and can be assumed to occur on the pathway to the didehydromethoxymethylene diradical (**III)**.

Using the geometries of the optimized S_0 state species and the S_1/S_0 C.I.s three reaction pathways were set up and optimized using the NEB method. The first pathway starts in the **I**-S_0-min geometry, propagates to the CI-asym geometry and arrives at the **II**-S_0-min geometry. The second pathway is the same as the former one, except the CI-asym-tw is used, i.e., **I**-S_0-min → CI-asym-tw → **II**-S_0-min. The two pathways correspond to breaking a lateral C-O bond and formation of acetaldehyde. The third pathway corresponds to breaking the basal C-C bond and propagates as **I**-S_0-min → CI-open → **III**-S_0-min.

For each of the three pathways, four MEPs were optimized using the NEB method with fixed endpoints:

(i) S_1 MEP from the **I** Franck-Condon (FC) point to the respective C.I.

(ii) S_0 MEP from the **I** equilibrium geometry to the respective C.I.

(iii) S_1 MEP from the respective C.I. to the respective product (**II** or **III**) FC geometry.

(iv) S_0 MEP from the respective C.I. to the respective product (**II** or **III**) equilibrium geometry.

For the first two reaction pathways (C2-O1 opening), the MEPs (i) and (ii) comprise 30 images and MEPs (iii) and (iv) comprise 40 images. For the last reaction pathway (C2-C3 opening), the MEPs (i) and (ii) comprise 60 images and the MEPs (iii) and (iv) comprises 20 images; the latter is due to geometric proximity of the CI-open and the **III**-S_0-min geometries.

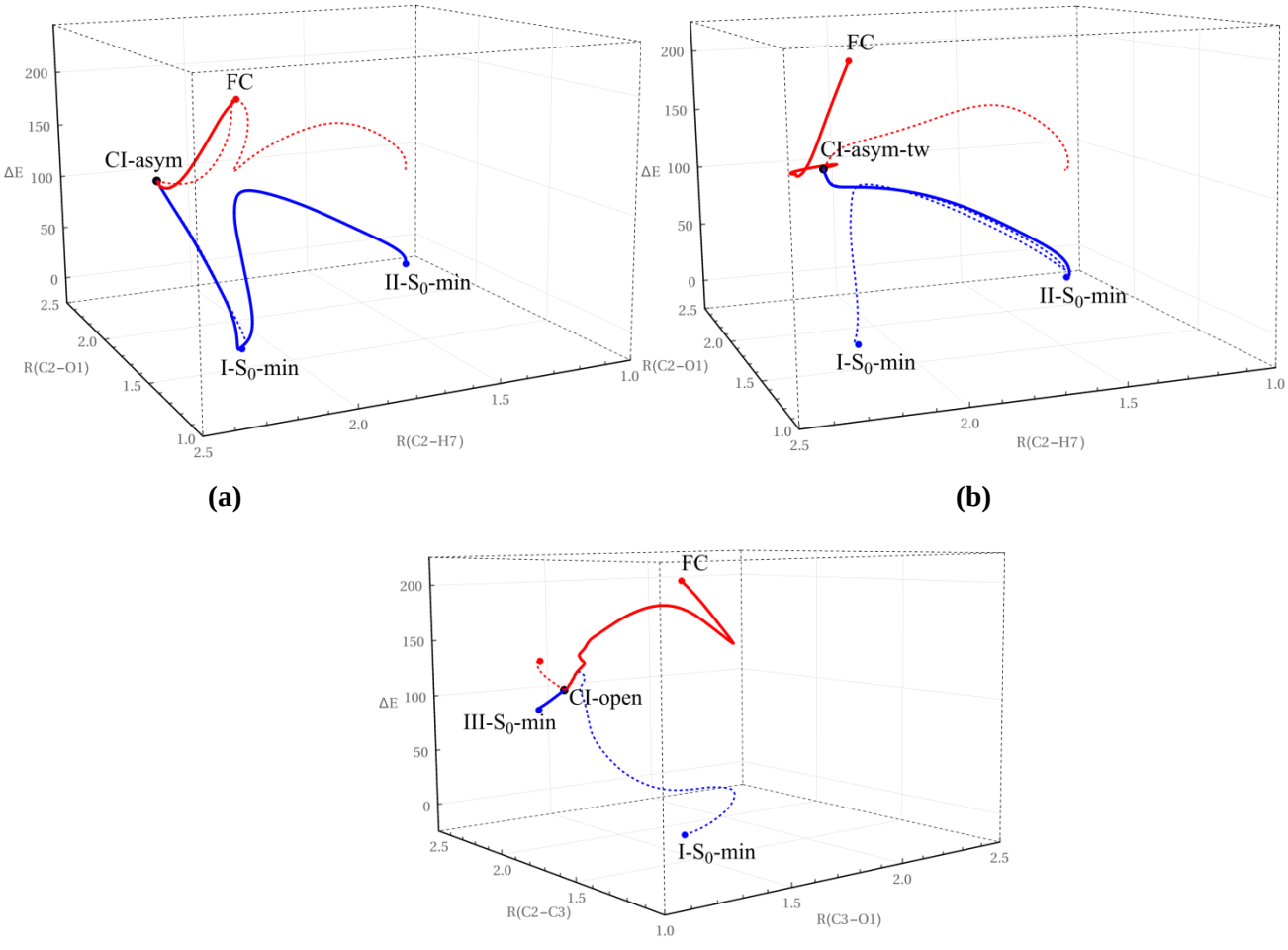

Figure 3. The relative energy ΔE (in kcal/mol) along the three oxirane ring opening paths corresponding to a lateral C-O bong breaking, **(a)** and **(b)**, and the basal C-C bond breaking, **(c)**; see **Figure 1** for more details. The solid red and blue lines represent the **I**-FC $\xrightarrow{S_1}$ CI and CI $\xrightarrow{S_0}$ **II**-S_0-min (or CI $\xrightarrow{S_0}$ **III**-S_0-min) branches, respectively. The dashed red and blue lines represent their respective S_0 (S_1) counterparts. The MEPs are shown in terms of the lengths of the bonds which undergo the greatest variation during the respective reaction.

The optimized reaction pathways are shown in **Figure 3**, where the relative energy ΔE, with respect to the **I**-S_0-min energy, are plotted as a function of the bond-lengths undergoing the greatest stretching/contraction during the respective reaction, i.e., the R(C2-O1) and R(C2-H7) for the C-O breaking pathways and the R(C3-O1) and R(C2-C3) for the C-C breaking pathway. The pathways corresponding to the photochemical ring opening reaction, *i.e.*, FC $\xrightarrow{S_1}$ C.I. $\xrightarrow{S_0}$ product (the superscript above the arrow denotes the PES on which the MEP propagates), are shown with the solid lines; their respective S_0 (S_1) counterparts with the dotted lines.

For the C-O breaking pathways, the S_1 MEPs start at the FC point of **I** proceed without hindrance to the respective C.I. point. This suggests that both C.I.s, CI-asym and CI-asym-tw, are easily accessible from the FC geometry and both can be equally involved with the ring opening mechanism.

For the C2-C3 opening pathway, the S_1 MEP features an intermediate minimum near the FC geometry. After passing the minimum, the S_1 MEP continues to CI-open, however its slope is noticeably less steep than for the C-O opening S_1 MEPs. The minimum on the C2-C3 opening S_1 MEP occurs due to the following: Initially, the MEP proceeds in the direction of the C3-O1 bond stretching and after reaching a length of 1.708 Å stretching of the C2-C3 bond commences. Hence, all three S_1 MEPs begin in approximately the same direction, a C-O (C2-O1 or C3-O1) bond stretching, and after a few steps, the C2-C3 opening MEP diverts to the respective C.I., which requires to overcame a barrier of ca. 34 kcal/mol, see **Figure 3(c)**. After crossing the CI-open, the S_0 MEP CI-open → **III**-S_0-min proceeds to the corresponding product without hindrance.

The S_0 MEPs CI $\overset{S_0}{\rightarrow}$ **II**-S_0-min of the two C2-O1 opening pathways behave differently from one another. The S_0 MEP CI-asym $\overset{S_0}{\rightarrow}$ **II**-S_0-min first returns back to the **I**-S_0-min geometry and only after that continues to acetaldehyde overcoming an S_0 barrier of 83 kcal/mol, see **Figure 3(a)**. This implies that there is an inclination of the S_0 PES near the CI-asym geometry which makes a direct propagation to acetaldehyde very unfavorable and enforces return to the reactant geometry. By contrast, the S_0 MEP CI-asym-tw $\overset{S_0}{\rightarrow}$ **II**-S_0-min proceeds to acetaldehyde without a hindrance.

A similarly peculiar observation also holds for the S_0 MEPs **I**-S_0-min $\overset{S_0}{\rightarrow}$ CI-asym and **I**-S_0-min $\overset{S_0}{\rightarrow}$ CI-asym-tw. The former MEP (blue dotted line in **Figure 3(a)**) goes from the S_0 equilibrium geometry directly to the CI-asym. The latter MEP (blue dotted in **Figure 3(b)**) first follows on the S_0 PES to the product (acetaldehyde) equilibrium geometry and only from there continues to the CI-asym-tw geometry. This suggests that performing torsion of the C2 methylene group necessary to reach CI-asym-tw on the S_0 PES is energetically more demanding then going to the product geometry. From the acetaldehyde equilibrium geometry the CI-asym-tw is reached without a hindrance.

Analysis of the C-O opening pathways suggests that there is a pronounced preference for the reaction product (oxirane or acetaldehyde) depending on the character of the C.I. which is crossed by the path. During the dynamics, the nuclear trajectories undergo the $S_1 \rightarrow S_0$ non-adiabatic transitions at the geometries on the C.I. seam not necessarily coinciding with the minimum energy C.I.s discussed above. Nevertheless, it can be conjectured that, when a C.I. close to the CI-asym geometry is crossed by the trajectory, oxirane, rather than acetaldehyde, should be the most likely product (aborted ring opening). Conversely, when the trajectory crosses a C.I. similar to CI-asym-tw, the ring opening reaction proceeds to acetaldehyde; the latter is likely to dissociate due to the large potential energy drop during the reaction. It is therefore desirable to investigate the origin of the difference in the respective pathways; firstly the S_1 branch

of the C2-C3 opening path, (see **Figure 3(c)**) vs. the S_1 branches of the C-O opening paths and secondly the S_0 branch of the CI-asym → **II**-S_0-min path vs. the CI-asym-tw → **II**-S_0-min path.

4.2. A QTAIM and stress tensor BCP analysis of the oxirane ring-opening reaction

In this section we quantify the chemical character of the C2-O1 *BCP*, C3-O1 *BCP* and C2-C3 *BCP* during the bond breaking processes for the three MEPs of the oxirane ring-opening photoreactions and the exchange of the H7 *NCP* between the C3 *NCP* and C2 *NCP*, see **Scheme 2** and **Figure 3**. The C.I. is indicated where practical, in the sub-figures of **Figure 4** by a vertical red line, otherwise it is stated in caption. We notice the contrasting locations of the C.I. for the three reaction pathways shown in the left, middle and right panels of sub-figure **(a)** of **Figure 4**.

The presence of a stronger and "stickier" closed-shell *BCP* is indicated by the presence of values of the total local energy density $H(\mathbf{r_b}) < 0$, see **Figure 4** and theory section 2.1. The C2-C3 *BCP*, C2-O1 *BCP* and C3-O1 *BCP*s for the CI-asym and CI-asym-tw MEPs in the S_0 state are generally stronger, on the basis of $H(\mathbf{r_b})$, than is the case for the S_1 state, see the left and middle panels of **Figure 4(a-c)** respectively. The exceptions are the C2-C3 *BCPs* for the **I**-S_0-min $\overset{S_0}{\rightarrow}$ CI-open and the **I**-FC $\overset{S_1}{\rightarrow}$ CI-open MEPs that are stronger in the S_1 than S_0 state before rupture. The S_0 and S_1 MEPs **I**-S_0-min $\overset{S_0}{\rightarrow}$ CI-open and **I**-FC $\overset{S_1}{\rightarrow}$ CI-open the shared-shell C2-O1 *BCP* both undergo a seemingly unusual chemical transformation to the shorter and stronger closed-shell C2-O1 *BCP* on the basis of more negative values of $H(\mathbf{r_b})$, see the right panel of **Figure 4(b)**. This chemical transformation also occurs for the C3-O1 *BCP* corresponding to the S_0 and S_1 MEPs **I**-S_0-min $\overset{S_0}{\rightarrow}$ CI-asym, **I**-FC $\overset{S_1}{\rightarrow}$ CI-asym, and **I**-S_0-min $\overset{S_0}{\rightarrow}$ CI-asym-tw, **I**-FC $\overset{S_1}{\rightarrow}$ CI-asym-tw MEPs, see the left and middle panels of **Figure 4(c)**. In both cases this is straightly forwardly explained by the C2-C3-O1 ring breaking in the **I**-S_0-min (**I**-FC) $\overset{S_0(S_1)}{\rightarrow}$ CI-open MEP, **I**-S_0-min (**I**-FC) $\overset{S_0(S_1)}{\rightarrow}$ CI-asym and **I**-S_0-min (**I**-FC) $\overset{S_0(S_1)}{\rightarrow}$ CI-asym-tw MEPs. Then the remaining 'dangling' C2-O1 BCP for the **I**-S_0-min (**I**-FC) $\overset{S_0(S_1)}{\rightarrow}$ CI-open and the C3-O1 *BCP* in the **I**-S_0-min (**I**-FC) $\overset{S_0(S_1)}{\rightarrow}$ CI-asym and **I**-S_0-min (**I**-FC) $\overset{S_0(S_1)}{\rightarrow}$ CI-asym-tw MEPs comprising the opened C2-C3-O1 ring exists in a different chemical environment. This is consistent with the more negative values of the stress tensor eigenvalue $\lambda_{3\sigma}$ that indicate a greater degree of instability and present for the closed-shell *BCP*s, almost all of the C2-O1 *BCPs* for the **I**-S_0-min (**I**-FC) $\overset{S_0(S_1)}{\rightarrow}$ CI-open $\overset{S_0(S_1)}{\rightarrow}$ **III**-S_0-min (**III**-FC) MEP are unstable on this basis.

The C2-C3 *BCP* bond-path remains intact for the entire **I**-S_0-min (**I**-FC) $\overset{S_0(S_1)}{\rightarrow}$ CI-asym $\overset{S_0(S_1)}{\rightarrow}$ **II**-S_0-min (**II**-FC) (left panel) and the **I**-S_0-min (**I**-FC) $\overset{S_0(S_1)}{\rightarrow}$ CI-asym-tw $\overset{S_0(S_1)}{\rightarrow}$ **II**-S_0-min (**II**-FC) (middle panel) MEPs but ruptures along the **I**-S_0-min (**I**-FC) $\overset{S_0(S_1)}{\rightarrow}$ CI-open before the C.I. (right panel), see **Figure 4(a)**. For the

I-S_0-min (**I**-FC) $\overset{S_0(S_1)}{\rightarrow}$ CI-open the shared-shell C2-C3 *BCP* ruptures catastrophically, i.e. without an intermediate closed-shell C2-C3 *BCP*, see the right panel of **Figure 4(a)**. The linear variation of the C2-C3 *BCP* bond-path length (BPL) for the S_0 and S_1 states along the **I**-S_0-min (**I**-FC) $\overset{S_0(S_1)}{\rightarrow}$ CI-open does not indicate the approaching C2-C3 *BCP* rupture. The variation of the eigenvector following path-length $\mathbb{H}$ along the MEP, demonstrates a deviation away from linearity before the C2-C3 *BCP* rupture, see the right panel of the **Supplementary Materials S6(a)**. The C2-O1 *BCP* and C3-O1 *BCP* do not rupture catastrophically. This is because the respective *BCP* annihilation occurs via the closed-shell C2--O1 *BCP*s, and closed-shell C3--O1 *BCP*, see the right panel of **Figure 4(c).** In addition we notice that the non-catastrophic annihilation is accompanied by increases in $\mathbb{H}$ an order of magnitude or more than for the catastrophic rupture of the shared-shell C2-C3 *BCP* for the **I**-S_0-min (**I**-FC) $\overset{S_0(S_1)}{\rightarrow}$ CI-open MEPs.

The bond-path of the C3-H7 *BCP* contracts and strengthens for the **I**-FC $\overset{S_1}{\rightarrow}$ CI-asym and **I**-FC $\overset{S_1}{\rightarrow}$ CI-asym-tw MEPs. Then both of the CI-asym $\overset{S_0}{\rightarrow}$ **II**-S_0-min and CI-asym-tw $\overset{S_0}{\rightarrow}$ **II**-S_0-min MEPs undergo an unusual bond-path contraction and weakening before the H7 *NCP* transfers from the C3 *NCP* to the C2 *NCP* forming the C2-H7 *BCP*, see the left and middle panel respectively of **Supplementary Materials S6(d**).

For the **I**-S_0-min $\overset{S_0}{\rightarrow}$ CI-asym-tw MEP the H7 *NCP* transfers twice between the C3 *NCP* and C2 *NCP*, this is indicated by the two blue circles in the middle panel of **Figure 4(d)**. There is no corresponding transfer of the H7 for the **I**-FC $\overset{S_1}{\rightarrow}$ CI-asym-tw MEP. For both the S_0 and S_1 states of the entire **I**-S_0-min (**I**-FC) $\overset{S_0(S_1)}{\rightarrow}$ CI-asym-tw $\overset{S_0(S_1)}{\rightarrow}$ **II**-S_0-min (**II**-FC) MEP the C2-C3-O1 ring does not reform once broken, see **Figure 5(a-b)** in section 4.3. Conversely, for both the S_0 and S_1 states of the **I**-S_0-min (**I**-FC) $\overset{S_0(S_1)}{\rightarrow}$ CI-asym $\overset{S_0(S_1)}{\rightarrow}$ **II**-S_0-min (**II**-FC) MEP the C2-C3-O1 ring reforms returning to the oxirane after breaking, see **Figure 4(a-b)**. The H7 *NCP* transfers between the C3 *NCP* and C2 *NCP* once for the CI-asym $\overset{S_0}{\rightarrow}$ **II**-S_0-min MEP, see the orange circle in the left panel of **Figure 4(d)**.

In section 4.3 we will attempt to explain a greater degree of *BCP* instability in the S_1 state is usually present compared with the S_0 state, as well as the mechanism of the H7 *NCP* transfer between the C3 *NCP* and C2 *NCP* see **Supplementary Materials S4(a-c)** respectively.

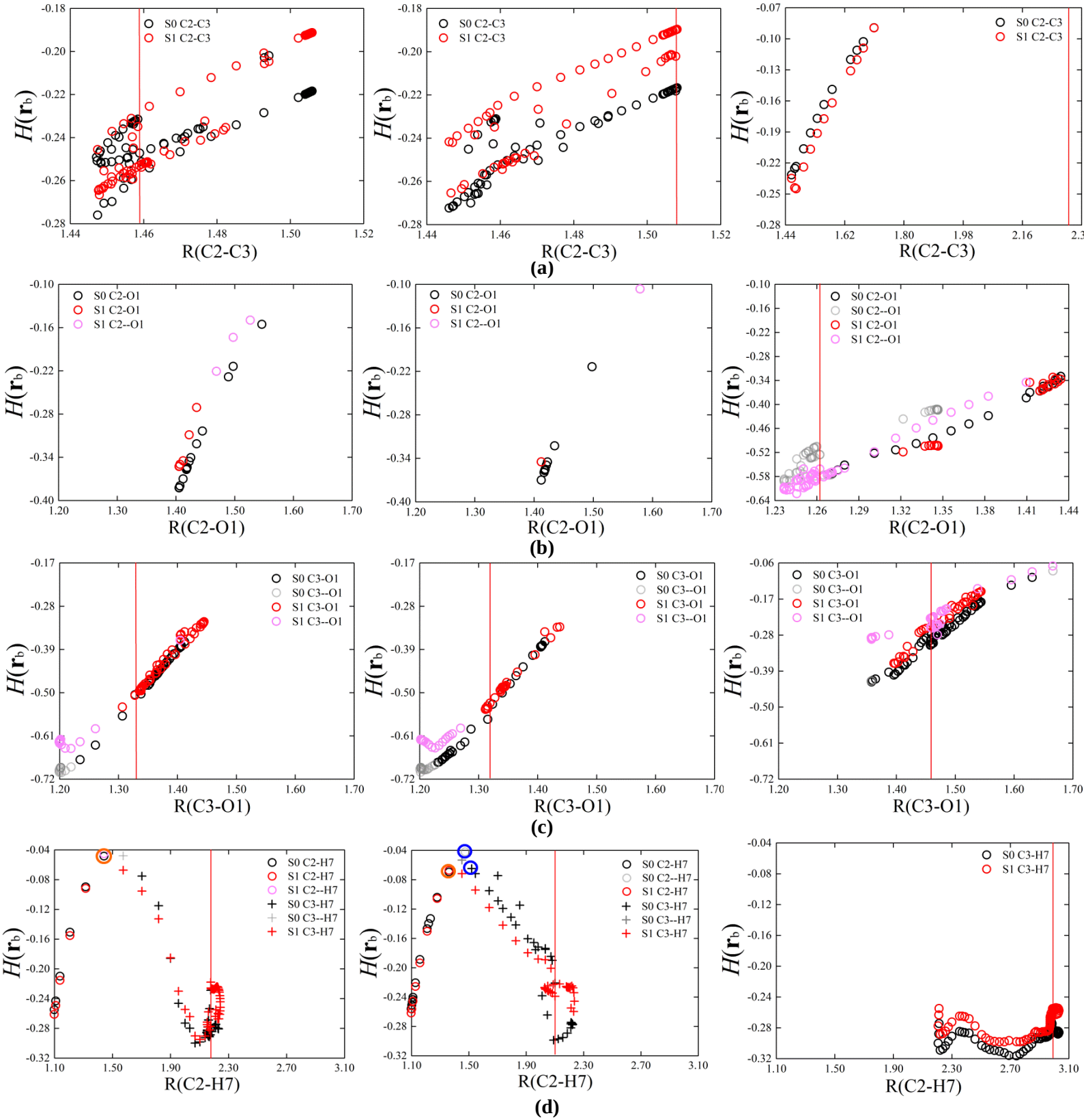

Figure 4. The variation of the total local energy density $H(\mathbf{r}_b)$ with the bond-path lengths(Å) associated with the C2-C3/C2--C3 *BCP*, C2-O1/C2--O1 *BCP*, C3-O1/C3--O1 *BCP* and C2-H7/C2--H7 *BCP* for the S_0 and S_1 states are presented in sub-figures **(a)-(d)** respectively. The **I**-S_0-min (**I**-FC) $\xrightarrow{S_0(S_1)}$ CI-asym $\xrightarrow{S_0(S_1)}$ **II**-S_0-min (**II**-FC), **I**-S_0-min (**I**-FC) $\xrightarrow{S_0(S_1)}$ CI-asym-tw $\xrightarrow{S_0(S_1)}$ **II**-S_0-min (**II**-FC) and **I**-S_0-min (**I**-FC) $\xrightarrow{S_0(S_1)}$ CI-open $\xrightarrow{S_0(S_1)}$ **III**-S_0-min (**III**-FC) pathways are presented in the left, middle and right panels respectively where the vertical red lines indicate the location of the CI and R(C2-O1) = 2.345 Å and R(C2-O1) = 2.226 Å for the CI-asym and CI-asym-tw respectively. The blue and orange circles shown on left and middle panels of sub-figure **(d)** represent the transfer of the H7 *NCP* between the C3 *NCP* and C2 *NCP* before and after the CI respectively in the S_0 state, see **Figure 5(a)** and **Figure 6(a)**.

4.3. A QTAIM 3-D bond-path analysis of three MEPs of the oxirane ring-opening reaction

In this section we present results from the 3-D QTAIM bond-path analysis along the dominant reaction paths for the three MEPs in the sub-figure **(a)** of each of **Figures 5-7**, that correspond to the solid red and solid blue lines for S_1 and S_0 states presented in **Figure 3**. The inverse paths are presented in the sub-figure **(b)** of each of **Figures 5-7** shown as the dashed red and dashed blue lines for S_1 and S_0 states also shown in **Figure 3**. The size, orientation and location of the {***q***,***q'***} path-packets indicate how much, which direction and whether a bond-path is twisted or linear, see the end of theory section 2.2 for further explanation. The greater strength and stability of C2-O1 *BCP* in the S_0 compared S_1 state as measured by the more negative values of $H(\mathbf{r_b})$ seen in the left and middle panels of **Figure 4(b)** is explained by the twisted S_0 C2-O1 *BCP* bond-path that will be less readily deformed in the plane of the C2-C3-O1 ring than the planar S_1 C2-O1 *BCP* bond-path.

The uniqueness of the **{*q*,*q'*}** path-packets is seen from a comparison of the reaction products CH_3CHO (**II**) or CH_2OCH_2 (**III**) shown in final sub-figures for each of the **(a) (b)** in **Figures 5-7**. Extremely long {***q***,***q'***} path-packets indicate the imminent rupture caused by the coalescence of a *BCP* with the associated *RCP*, e.g. for the bond-path of C2-O1 *BCP* presented in the second sub-figure of **Figure 5(b)**.

Differences in the major and inverse MEPs on the {***q***,***q'***} path-packets can be seen by a comparison of the **(a)** and **(b)** sub-figures for each of **Figures 5-7** respectively. The {***q***,***q'***} path-packets associated with the **I**-FC $\overset{S_1}{\rightarrow}$ CI-asym $\overset{S_0}{\rightarrow}$ **II**-S_0-min (the major pathway) corresponding to the solid red and solid blue lines for S_1 and S_0 states presented in **Figure 3(a)** and **Figure 5(a).** The {***q***,***q'***} path-packets from the major pathway are contrast with those of the counterpart path **I**-S_0-min $\overset{S_0}{\rightarrow}$ CI-asym $\overset{S_1}{\rightarrow}$ **II**-FC, **see Figure 5(b)** and the dashed red and dashed blue lines in **Figure 3(a).** The behavior of the {***q***,***q'***} path-packets in **Figure 5(a)** corresponds to the downhill major path and in **Figure 5(b)** to the counterpart uphill path. This is because the planar C2-O1 *BCP* bond-path for the S_1 **I**-FC indicates an easier C2-C3-O1 ring-opening than for the torsional C2-O1 *BCP* bond-path for the **I**-S_0-min, compare the first sub-figures of **Figure 5(a)** and **Figure 5(b)** respectively. Note that the planar C2-O1 *BCP* bond-path is due to the elongated {***q***,***q'***} path-packets along the entire bond-path and the torsional C2-O1 *BCP* bond-path is due to the presence of orthogonal {***q***,***q'***} path-packets either side of the C2-O1 *BCP*.

The C2-C3-O1 ring opens for the CI-asym $\overset{S_0}{\rightarrow}$ **II**-S_0-min leg of the major path which is more favorable than the inverse path CI-asym $\overset{S_1}{\rightarrow}$**II**-FC, comparing **Figure 5(a)** and **Figure 5(b)** respectively. This is because the twisted bond-path maintains a sizable **{*q*,*q'*}** path-packet around the C2-O1 *BCP* that causes the C2-C3-O1 ring to reclose. When we compare with the more favorable CI-asym-tw $\overset{S_0}{\rightarrow}$ **II**-S_0-min leg of the major pathway we see that the C2-C3-O1 ring does not reclose because of the absence of a sizable **{*q*,*q'*}** path-packet in vicinity of the C2-O1 *BCP* bond-path, see **Figure 6(a)**.

Similar behavior is seen for the **I**-FC $\overset{S_1}{\rightarrow}$ CI-asym-tw (the major pathway) and the **I**-S_0-min $\overset{S_0}{\rightarrow}$

CI-asym-tw counterpart pathways, see **Figure 6(a)** and **Figure 6(b)** respectively. The difference is that use of the twisted H4-C2-H5 group in the CI-asym-tw the C2-C3-O1 ring prevents the C2-O1 *BCP* bond-path rotated around to reclose the once opened C2-C3-O1 ring.

After the O1 *NCP* has moved the C3-O1 *BCP* bond-path reacquires the torsion and then the C2-O1 *BCP* reforms closing the ring, before rupturing again, see the fifth to eighth sub-figures of **Figure 5(a)**. The O1 *NCP* and the H7 *NCP* both move and the imminent rupture of the C3-H7 *BCP* is indicated by the extremely long associated {***q***,***q'***} path-packet before transfer of the H7 *NCP* to the C2 *NCP* to form the C2-H7 *BCP* and the product acetaldehyde in the S_0 state, see the final sub-figure of **Figure 5(a)** and **Figure 5(b)**.

For the corresponding {***q***,***q'***} path-packet in the S_1 state a lack of torsion of the C2-O1 *BCP* and C3-O1 *BCP* bond-paths are indicated by two perpendicular {***q***,***q'***} path-packets, is observed, e.g. see the oxirane (first sub-figure) of **Figure 5(b)**, **Figure 6(b)** and **Figure 7(b).** Again, as was observed for the S_0 state, imminent *BCP* rupture is indicated by the formation of a large {***q***,***q'***} path-packet around the *BCP* and the motion of a bond-path and hence the associated *NCP* and *BCP* is indicated by a large {***q***,***q'***} path-packet close to the *NCP*, e.g. the second and fourth sub-figures of **Figure 6(b)** respectively.

Now we consider the C2-C3 bond opening pathway, **I**-FC $\overset{S_1}{\rightarrow}$ CI-open $\overset{S_0}{\rightarrow}$ **III**-S_0-min (CH_2CH_2O), see the sixth sub-figures in both of **Figure 7(a)** (major pathway) and **Figure 7(b)** (inverse pathway). The large {***q***,***q'***} path-packet around the C2-C3 *BCP* also includes the neighboring *RCP* that will coalesce and annihilate the *RCP* and the C2-C3 *BCP.* We see a similar annihilation process the C3-O1 *BCP* bond-path, see the second sub-figures in both of **Figure 7(a)** and **Figure 7(b)**. For both the major and minor pathways; **I**-S_0-min (**I**-FC) $\overset{S_0(S_1)}{\rightarrow}$ CI-open the C2-C3-O1 ring closes and reopens due to the instability of the C3-O1 *BCP* bond-path.

For the S_1 state we see ring-closing occurring after and before the respective C.I.s are reached for the **I**-FC $\overset{S_1}{\rightarrow}$ CI-asym $\overset{S_0}{\rightarrow}$ **II**-S_0-min (CH_3CHO) and **I**-FC $\overset{S_1}{\rightarrow}$ CI-open MEPs, see **Figure 5(b)** and **Figure 7(b)** respectively. For the **I**-FC $\overset{S_1}{\rightarrow}$ CI-open however the C2-C3 *BCP* is very unstable as can be seen by the large {***q***,***q'***} path-packet around the C2-C3 *BCP* and the proximity of the *RCP.* For the minor pathway the very long thin {***q***,***q'***} path-packets associated with C2-O1 *BCP* and C3-O1 *BCP* indicate the direction of the very strong tendency for the O1 *NCP* to move, see the seventh sub-figure of **Figure 7(b)**. The final sub-figure also shows a similar tendency of for the {***q***,***q'***} path-packets C3-O1 *BCP* in contrast to the final sub-figure of the major pathway, compare **Figure 7(a)** and **Figure 7(b)**.

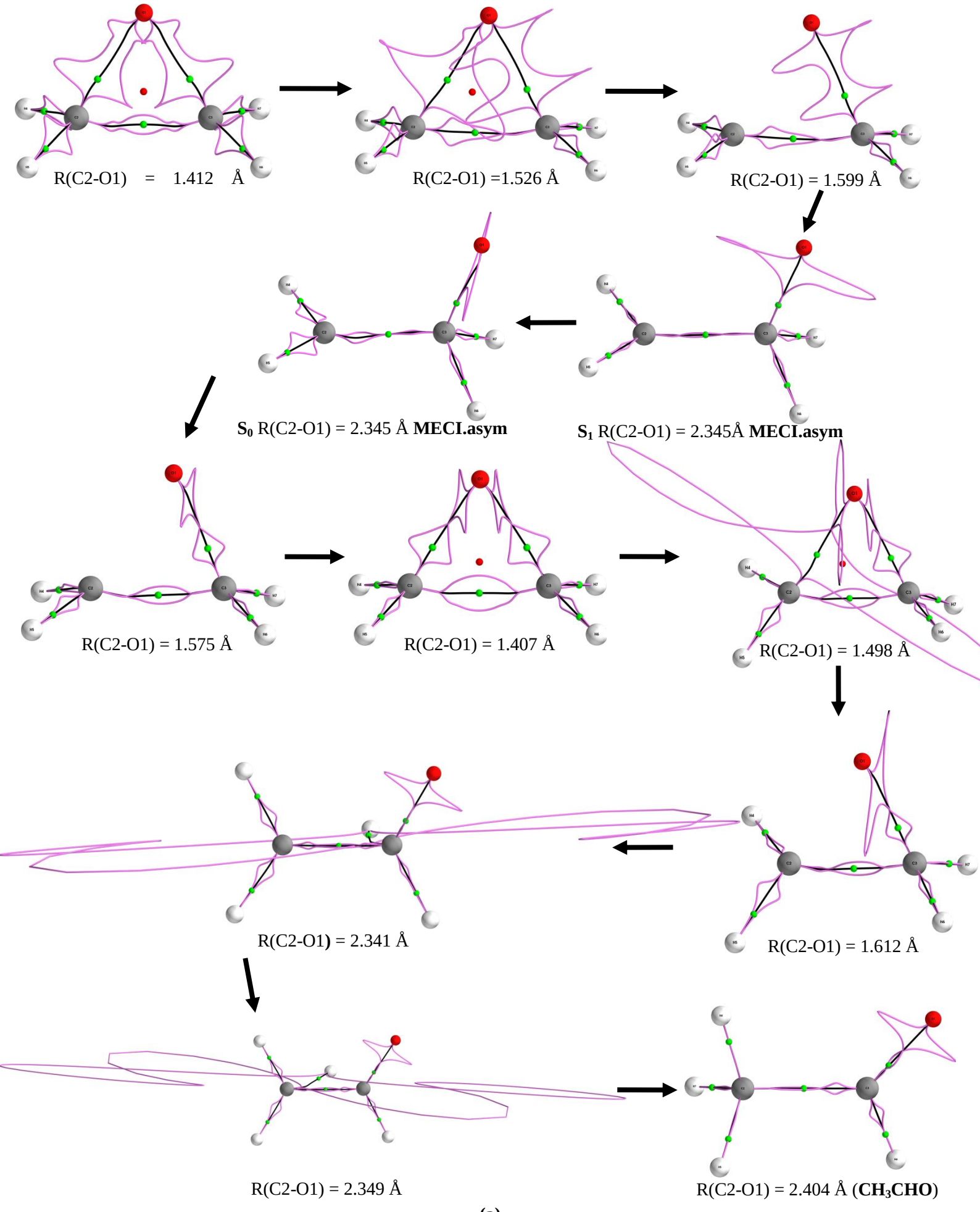
R(C2-O1) = 1.412 Å
R(C2-O1) =1.526 Å
R(C2-O1) = 1.599 Å
S0 R(C2-O1) = 2.345 Å MECI.asym
S1 R(C2-O1) = 2.345Å MECI.asym
R(C2-O1) = 1.575 Å
R(C2-O1) = 1.407 Å
R(C2-O1) = 1.498 Å
R(C2-O1) = 2.341 Å
R(C2-O1) = 1.612 Å
R(C2-O1) = 2.349 Å
R(C2-O1) = 2.404 Å (CH3CHO)

(a)

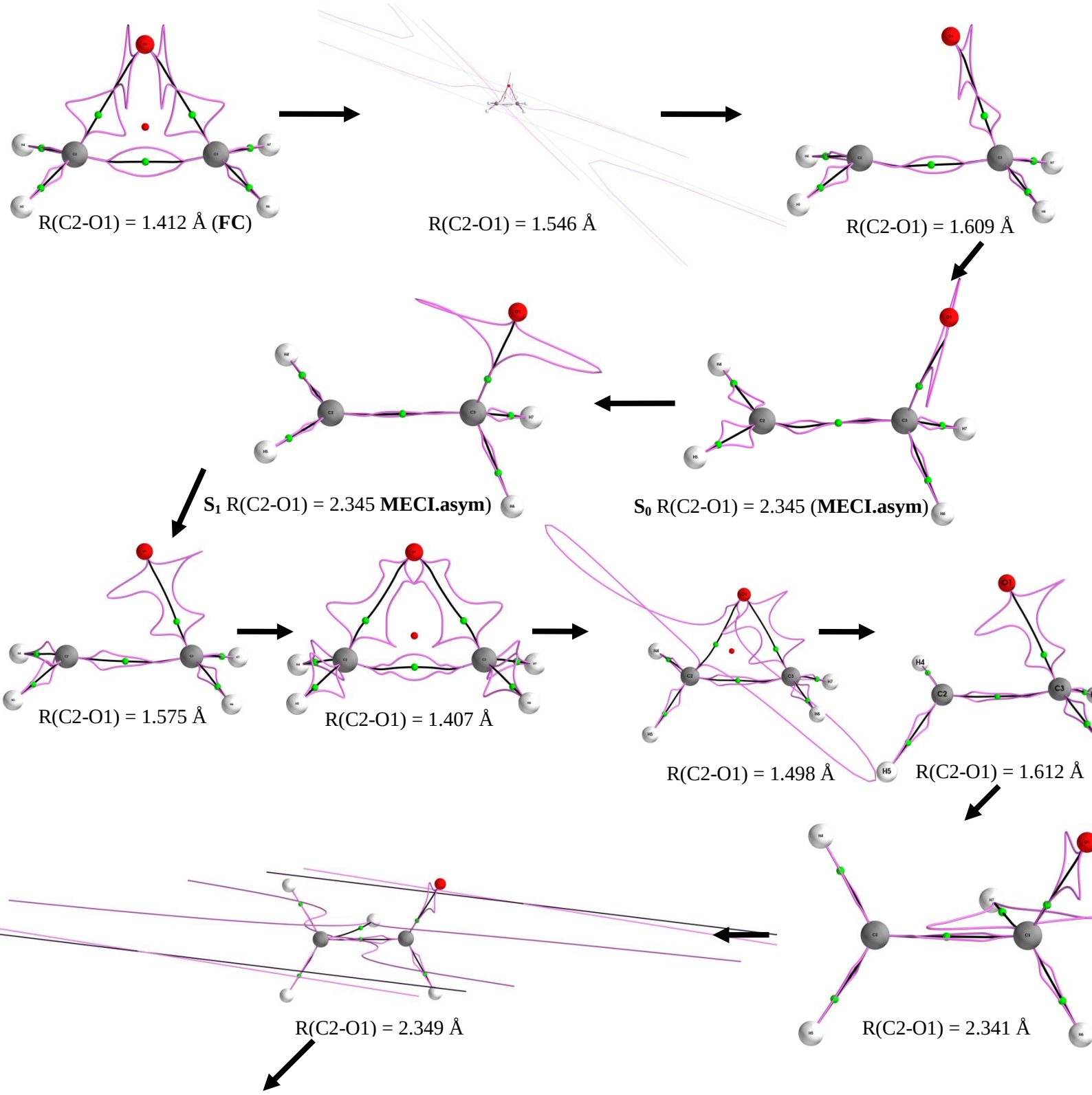

Figure 5. A selection of the {***q***,***q'***} path-packets, see the theory section 2.2 and section 4.3, are indicated by the magenta lines corresponds to the **I**-FC $\xrightarrow{S_1}$ CI-asym followed by the CI-asym $\xrightarrow{S_0}$ **II**-S_0-min branches in sub-figure **(a)** indicated by the solid red and solid blue lines shown respectively in **Figure 3.** In sub-figure **(b)** the inverse path **I**-S_0-min $\xrightarrow{S_0}$ CI-asym followed by the CI-asym $\xrightarrow{S_1}$ **II**-FC branches indicated by the dashed red and dashed blue lines respectively in **Figure 3.** We present the {***q***,***q'***} path-packets CI for both the S_0 and S_1 states.

(b)

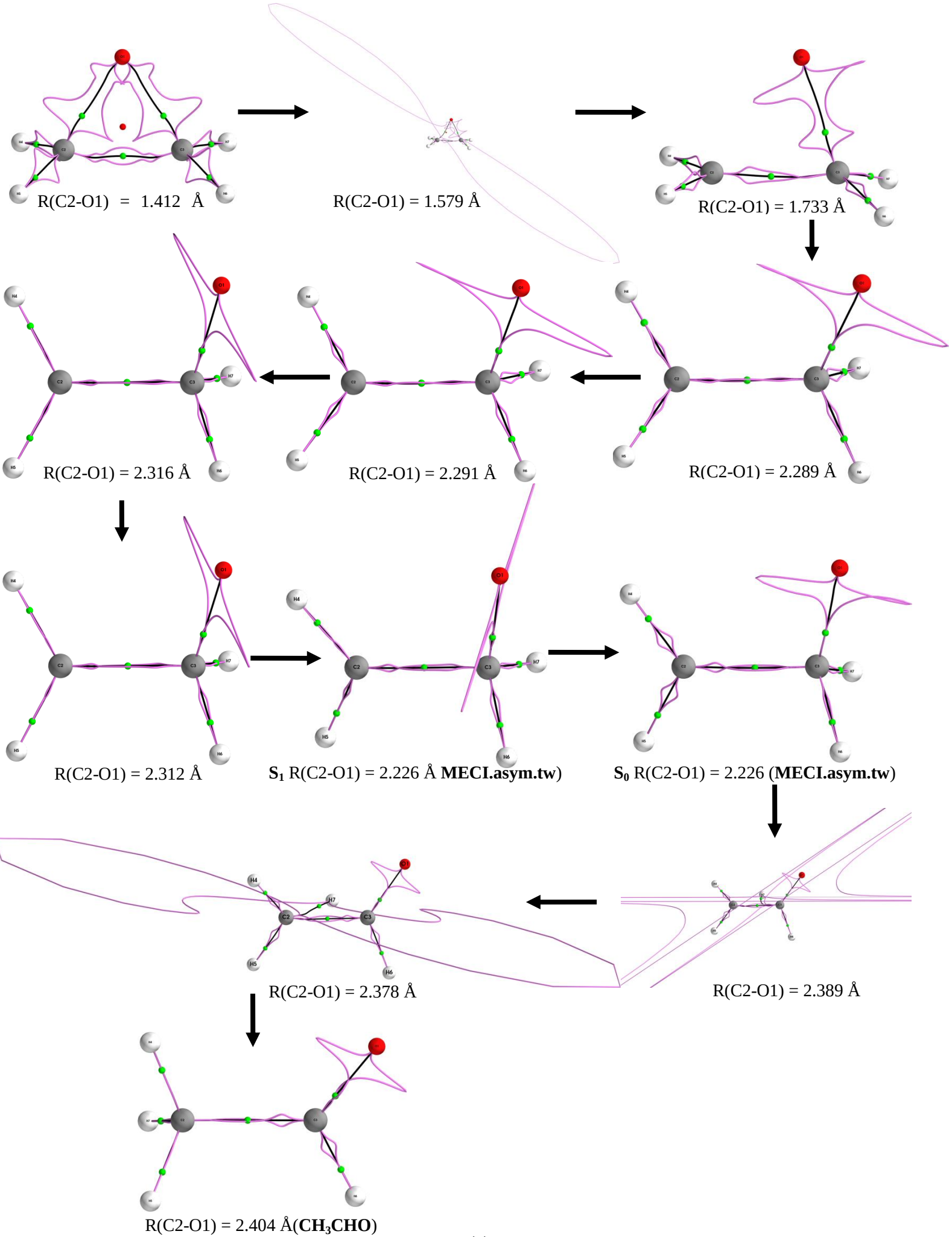
R(C2-O1) = 1.412 Å
R(C2-O1) = 1.579 Å
R(C2-O1) = 1.733 Å
R(C2-O1) = 2.316 Å
R(C2-O1) = 2.291 Å
R(C2-O1) = 2.289 Å
R(C2-O1) = 2.312 Å
S1 R(C2-O1) = 2.226 Å MECI.asym.tw)
S0 R(C2-O1) = 2.226 (MECI.asym.tw)
R(C2-O1) = 2.389 Å
R(C2-O1) = 2.378 Å
R(C2-O1) = 2.404 Å(CH3CHO)

(a)

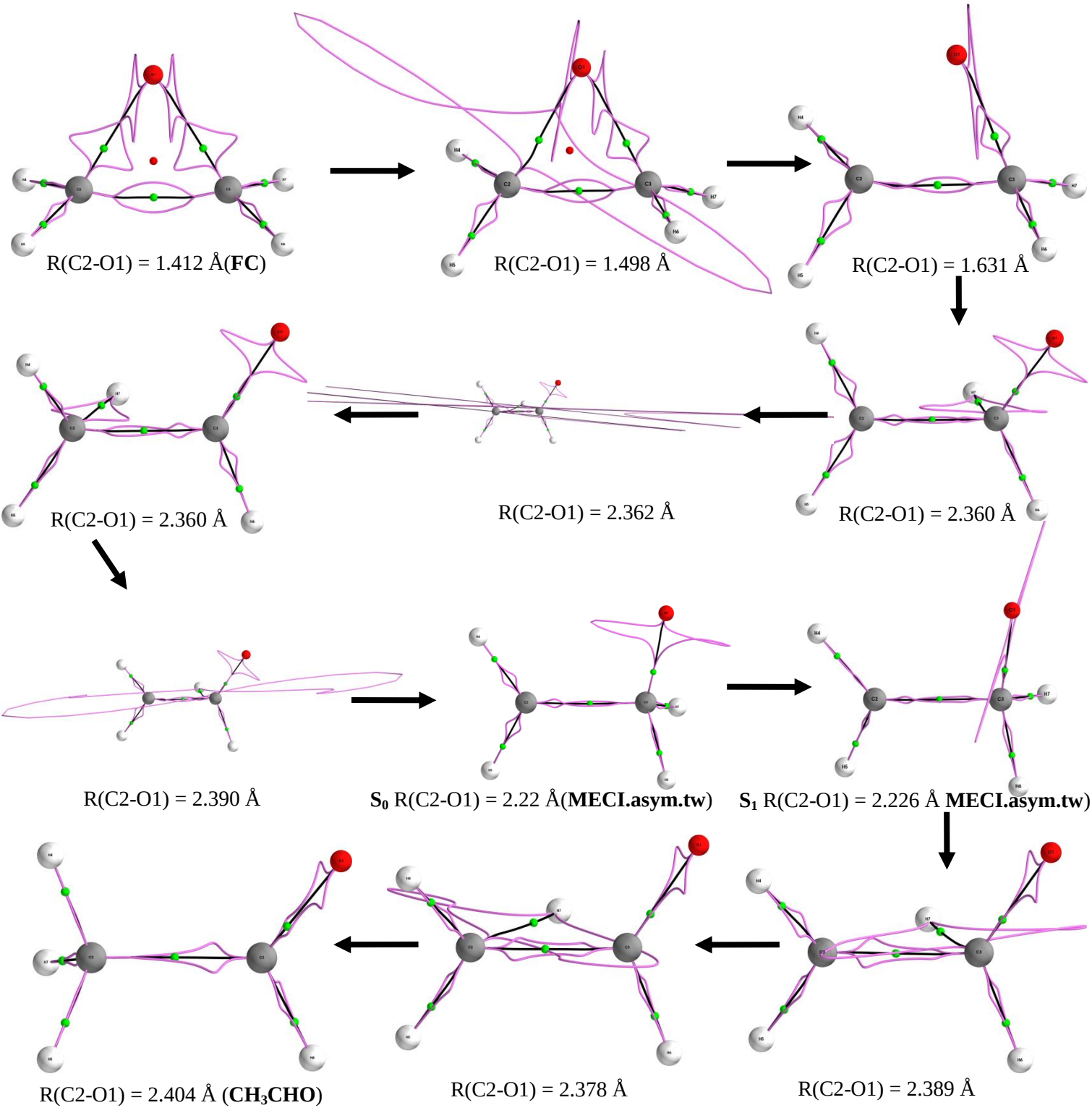

(b)

Figure 6. A selection of the {***q***,***q'***} path-packets correspond to the **I**-FC $\xrightarrow{S_1}$ CI-asym-tw followed by the CI-asym-tw $\xrightarrow{S_0}$ **II**-S_0-min branches in sub-figure **(a)** indicated by the solid red and solid blue lines shown respectively in **Figure 3.** In sub-figure **(b)** the inverse path **I**-S_0-min $\xrightarrow{S_0}$ CI-asym-tw followed by the CI-asym-tw $\xrightarrow{S_1}$ **II**-FC branches indicated by the dashed red and dashed blue lines respectively in **Figure 3**, see the caption of **Figure 5** for further details.

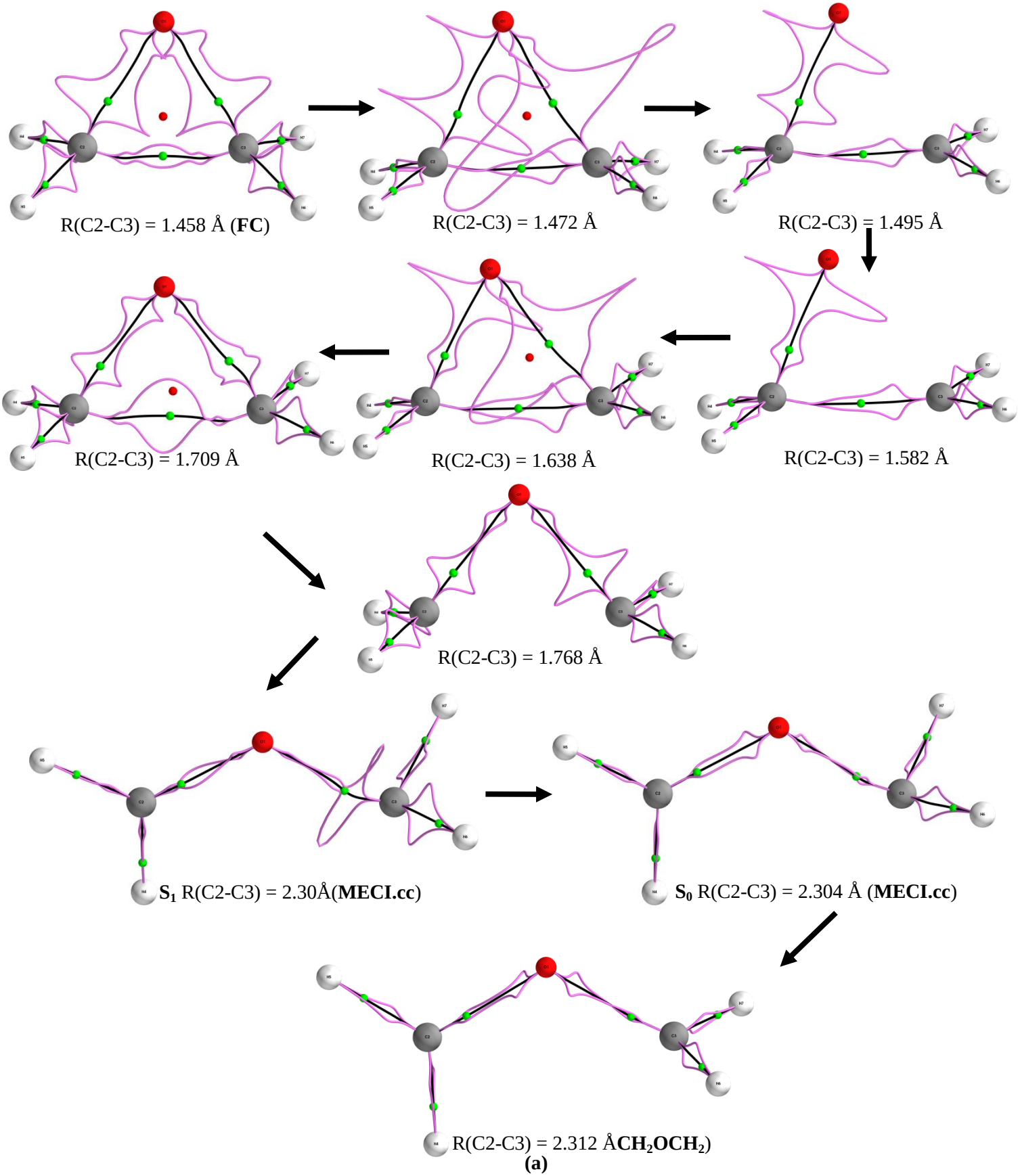
R(C2-C3) = 1.458 Å (**FC**)
R(C2-C3) = 1.472 Å
R(C2-C3) = 1.495 Å
R(C2-C3) = 1.582 Å
R(C2-C3) = 1.638 Å
R(C2-C3) = 1.709 Å
R(C2-C3) = 1.768 Å
S₁ R(C2-C3) = 2.30Å(**MECI.cc**)
S₀ R(C2-C3) = 2.304 Å (**MECI.cc**)
R(C2-C3) = 2.312 Å**CH₂OCH₂**)

(a)

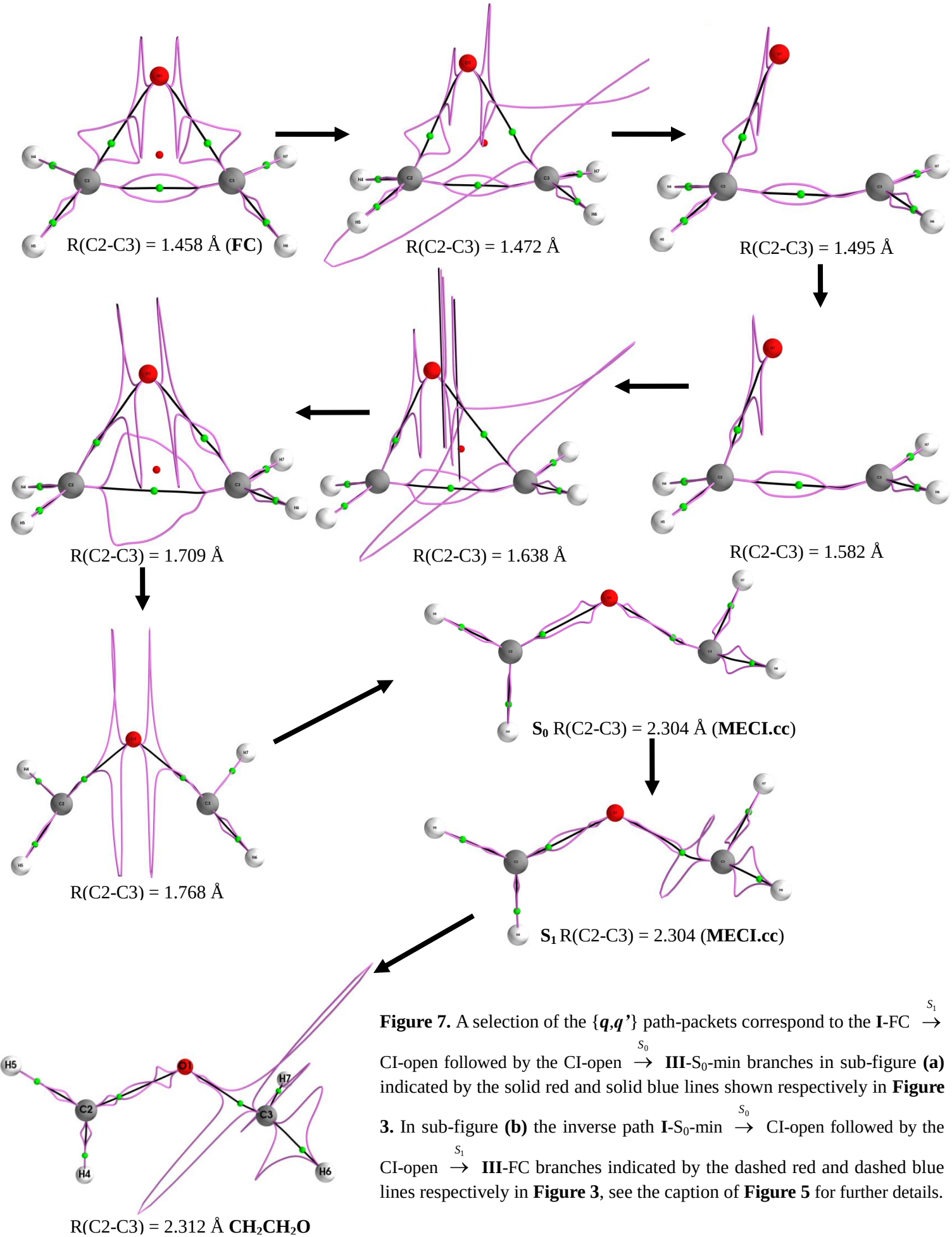

Figure 7. A selection of the {***q***,***q'***} path-packets correspond to the **I**-FC $\xrightarrow{S_1}$ CI-open followed by the CI-open $\xrightarrow{S_0}$ **III**-S_0-min branches in sub-figure **(a)** indicated by the solid red and solid blue lines shown respectively in **Figure 3.** In sub-figure **(b)** the inverse path **I**-S_0-min $\xrightarrow{S_0}$ CI-open followed by the CI-open $\xrightarrow{S_1}$ **III**-FC branches indicated by the dashed red and dashed blue lines respectively in **Figure 3**, see the caption of **Figure 5** for further details.

(b)

Conclusions

We used QTAIM and the stress tensor analysis to explain firstly differences in the S_1 branches of the C-C opening path compared with the corresponding C-O opening paths.

Secondly, we explained the less unfavorable ring-ringing behavior in the CI-asym $\overset{S_0}{\rightarrow}$ **II**-S_0-min and the CI-asym-tw $\overset{S_0}{\rightarrow}$ **II**-S_0-min pathways by examining changes to the directions of the {***q***,***q,'***} path-packet, the 3-D paths that define the most preferred direction of electronic motion. The C2-C3-O1 ring once opened remained opened for the CI-asym-tw $\overset{S_0}{\rightarrow}$ **II**-S_0-min pathway due to the torsion of the H4-C2-H5 group present being transmitted down the central C2-C3 *BCP* bond-path and affecting the torsion of the C3-O1 *BCP* bond-path. These changes in torsion of the C2-C3 *BCP* bond-path and C3-O1 *BCP* bond-path facilitated the transfer of the H7 *NCP* between the C3 *NCP* and C2 *NCP* that occurred twice in the **I**-S_0-min $\overset{S_0}{\rightarrow}$ CI-asym-tw. No transfer of the H7 *NCP* occurred for the S_0-min $\overset{S_0}{\rightarrow}$ CI-asym. In addition, no transfer of the H7 *NCP* for the either the major or inverse C2-C3 *BCP* bond-path rupturing pathways that lead to CH_2CH_2O where the ring also recloses when opened.

The {***q***,***q,'***} path-packet demonstrated differences in the topology of a given bond-path as linear or twisted and the imminent rupture of a *BCP* or movement of a bond-path and associated *BCP* and *NCP*s. The shared-shell C2-C3 *BCP* rupture mechanism for the major and inverse CI-open $\overset{S_0(S_1)}{\rightarrow}$ **III**-S_0-min (**III**-FC) pathways proceeded without first transforming to a closed-shell *BCP* and therefore was referred to as a *catastrophic* rupture. The C2-C3 *BCP* bond-path was not twisted in either of the S_0 and S_1 states. In addition, for the C2-C3 *BCP* rupture the {***q***,***q'***} path-packet were longer and weaker in the S_0 compared with S_1 state. This indicated the unfavored nature of the inverse pathway compared with major pathway; **I**-FC $\overset{S_1}{\rightarrow}$ CI-open $\overset{S_0}{\rightarrow}$ **III**-S_0-min. Neither of the C2-O1 *BCP* bond-path rupturing process that occurred along the major pathways **I**-FC $\overset{S_1}{\rightarrow}$ CI-asym and **I**-FC $\overset{S_1}{\rightarrow}$ CI-asym-tw were catastrophic. The inverse pathways; **I**-S_0-min $\overset{S_0}{\rightarrow}$ CI-asym and **I**-S_0-min $\overset{S_0}{\rightarrow}$ CI-asym-tw however, did comprise a catastrophic C2-O1 *BCP* bond-path rupturing process.

We found that for the **I**-S_0-min the C2-O1 *BCP* bond-path was twisted from inspection of the {***q***,***q'***} path-packets and generally the C2-O1 *BCP* and C3-O1 *BCP* bond-paths possessed a degree of torsion for the entirety of the three pathways in the S_0 state. Conversely, none of the corresponding bond-paths were found to be twisted in the S_1 state and were all found to be linear. This was explained by the planar topology of the {***q***,***q,'***}-paths of the C2-O1 *BCP* in the S_1 state are and facilitated the sliding open of the C3-O1 *BCP* bond-path.

Acknowledgements

The National Natural Science Foundation of China is gratefully acknowledged, project approval number: 21673071. The One Hundred Talents Foundation of Hunan Province is also gratefully acknowledged for the support of S.J. and S.R.K.

References

1. R. Gomer and W. A. Noyes, *J. Am. Chem. Soc.*, **1950**, 72, 101–108.
2. M. Kawasaki, T. Ibuki, M. Iwasaki and Y. Takezaki, *Chem. Phys. - CHEM PHYS*, **1973**, 59, 2076–2082.
3. B. Bigot, A. Sevin and A. Devaquet, *J. Am. Chem. Soc.*, **1979**, 101, 1095–1100.
4. B. Bigot, A. Sevin and A. Devaquet, *J. Am. Chem. Soc.*, **1979**, 101, 1101–1106.
5. R. Huisgen, *Angew. Chem.-Int. Ed. - ANGEW CHEM INT ED*, **1977**, 16, 572–585.
6. M. C. Flowers and D. E. Penny, *J Chem See Faraday Trans 1*, **1974**, 70, 355–361.
7. G. A. Lee, *J. Org. Chem.*, **1976**, 41, 2656–2658.
8. F. Cordova, L. J. Doriol, A. Ipatov, M. E. Casida, C. Filippi & A. *J.* Vela, *Chem. Phys.* **127**, 164111 (2007).
9. E. Tapavicza, I. Tavernelli, U. Rothlisberger, C. Filippi and M. E. Casida, *J. Chem. Phys.*, **2008**, 129, 124108.
10. M. Huix-Rotllant, B. Natarajan, A. Ipatov, C.M. Wawire, T. Deutsch & M.E. Casida, *Phys. Chem. Chem. Phys.* **12**, 12811–12825 (2010).
11. J.-H. Li, T. Zuehlsdorff, M. Payne and N. Hine, *Phys Chem Chem Phys*, **2015**, 17.
12. T. Tian, T. Xu, S. R. Kirk, M. Filatov and S. Jenkins, *Chem. Phys. Lett.*, **2019**, 717, 91–98.
13. T. Tian, T. Xu, S. R. Kirk, M. Filatov and S. Jenkins, *Int. J. Quantum Chem.*, **2019**, 119, e25862.
14. M. A. Blanco, A. Martín Pendás and E. Francisco, *J. Chem. Theory Comput.*, **2005**, 1, 1096–1109.
15. T. Xu, J. Farrell, Y. Xu, R. Momen, S.R. Kirk, S. Jenkins & D.J. Wales, *J. Comput. Chem.* **37**, 2712–2721 (2016).
16. R. F. W. Bader, *Atoms in Molecules: A Quantum Theory*, Oxford University Press, USA, **1994**.
17. R. F. W. Bader, *J. Phys. Chem. A*, **1998**, 102, 7314–7323.
18. R. F. W. Bader, *J. Phys. Chem. A*, **2009**, 113, 10391–10396.
19. P. W. Ayers and S. Jenkins, *J. Chem. Phys.*, **2009**, 130, 154104-154104–11.
20. S. Jenkins, S. R. Kirk, A. S. Cote, D. K. Ross and I. Morrison, *Can. J. Phys.*, **2003**, 81, 225-231(7).
21. R. G. A. Bone and R. F. W. Bader, *J. Phys. Chem.*, **1996**, 100, 10892–10911.
22. J. R. Maza, S. Jenkins and S. R. Kirk, *Chem. Phys. Lett.*, **2016**, 652, 112–116.
23. S. Jenkins, L. Blancafort, S. R. Kirk and M. J. Bearpark, *Phys. Chem. Chem. Phys.*, **2014**, 16, 7115–7126.
24. E. Kraka and D. Cremer, *J. Mol. Struct. THEOCHEM*, **1992**, 255, 189–206.
25. S. Jenkins and M. I. Heggie, *J. Phys. Condens. Matter*, **2000**, 12, 10325–10333.
26. S. Jenkins and I. Morrison, *Chem. Phys. Lett.*, **2000**, 317, 97–102.
27. J. H. Li, W. J. Huang, T. Xu, S. R. Kirk and S. Jenkins, *Int. J. Quantum Chem.*, **2018**, 119, e25847.
28. M. Filatov, *Wiley Interdiscip. Rev. Comput. Mol. Sci.*, **2015**, 5, 146–167.
29. M. Filatov, *Density-Funct. Methods Excit. States*, **2015**, 97–124.
30. M. Filatov, F. Liu and T. J. Martínez, *J. Chem. Phys.*, **2017**, 147, 034113.
31. M. Huix-Rotllant, M. Filatov, S. Gozem, I. Schapiro, M. Olivucci & N. Ferré, *J. Chem. Theory Comput.* **9**, 3917–3932 (2013).
32. A. Nikiforov, J. A. Gamez, W. Thiel, M. Huix-Rotllant and M. Filatov, *J. Chem. Phys.*, **2014**, 141, 124122.
33. M. Huix-Rotllant, A. Nikiforov, W. Thiel and M. Filatov, in *Density-Functional Methods for Excited States*, eds. N. Ferré, M. Filatov and M. Huix-Rotllant, Springer International Publishing, Cham, **2016**, pp. 445–476.
34. M. A. Rohrdanz, K. M. Martins and J. M. Herbert, *J. Chem. Phys.*, **2009**, 130, 054112.
35. R. Krishnan, J. S. Binkley, R. Seeger and J. A. Pople, *J. Chem. Phys.*, **1980**, 72, 650–654.
36. I. S. Ufimtsev and T. J. Martínez, *J. Chem. Theory Comput.*, **2008**, 4, 222–231.
37. I. S. Ufimtsev and T. J. Martinez, *J. Chem. Theory Comput.*, **2009**, 5, 1004–1015.
38. I. S. Ufimtsev and T. J. Martinez, *J. Chem. Theory Comput.*, **2009**, 5, 2619–2628.
39. I. S. Ufimtsev and T. J. Martínez, *Comput. Sci. Eng.*, **2008**, 10, 26–34.
40. A. V. Titov, I. S. Ufimtsev, N. Luehr and T. J. Martinez, *J. Chem. Theory Comput.*, **2013**, 9, 213–221.
41. J. Kästner, J.M. Carr, T.W. Keal, W. Thiel, A. Wander & P. *J.* Sherwood, *Phys. Chem. A* **113**, 11856–11865

(2009).
42. B. G. Levine, J. D. Coe and T. J. Martínez, *J. Phys. Chem. B*, **2008**, 112, 405–413.
43. H. Jónsson, G. Mills and K. W. Jacobsen, in *Classical and Quantum Dynamics in Condensed Phase Simulations*, WORLD SCIENTIFIC, **1998**, pp. 385–404.
44. G. Graner, E. Hirota, T. Iijima, K. Kuchitsu, D. A. Ramsay, J. Vogt and N. Vogt, in *Inorganic Molecules*, ed. K. Kuchitsu, Springer Berlin Heidelberg, Berlin, Heidelberg, **1998**, pp. 27–117.
45. H. Hollenstein and H. H. Günthard, *Spectrochim. Acta Part Mol. Spectrosc.*, **1971**, 27, 2027–2060.